Engineered Nanofunctional Thin Films as Interfacial Layers to Enhance Performance and Durability of SOFCs

ECS Transactions, 111 (6) 1453-1462 (2023)
10.1149/11106.1453ecst ©The Electrochemical Society

Engineered Nanofunctional Thin Films as Interfacial Layers to Enhance Performance and Durability of SOFCs

M. Machado[a], F. Baiutti[b], L. Bernadet[b], A. Morata[b], M. Nuñez[b], J. P. Ouweltjes[c], F. C. Fonseca[a], M. Torrell[b], and A. Tarancón[bd]

[a] IPEN-CNEN, Nuclear and Energy Research Institute, 05508-000, São Paulo, SP, Brazil
[b] Catalonia Institute for Energy Research (IREC), Department of Advanced Materials for Energy, Jardins de les Dones, 1, 08930 Sant Adrià de Besòs, Barcelona, Spain
[c] SolydEra SpA, Viale Trento 117, Mezzolomardo, 38017, Italy
[d] ICREA, Passeig Lluís Companys 23, 08010 Barcelona, Spain

A strategy to improve the performance and durability of solid oxide fuel cells (SOFCs) is to increase the cathodic activity and decrease the interfacial resistance between the cathode and electrolyte. Pulsed laser deposition (PLD) has been shown to be a promising method to engineer functional interlayers to enhance the cell's performance. In the present study, a bilayer consisting of $Sm_{0.2}Ce_{0.8}O_{2-\delta}$ (SDC) barrier layer (BL) and a nanocomposite consisting of SDC-$La_{0.8}Sr_{0.2}MnO_{3-\delta}$ (SDC-LSM) employed as a cathode functional layer were deposited by PLD in an anode supported SOFC. The fuel cell showed maximum power density of 0.30 $W \cdot cm^{-2}$ at 750 °C. Most importantly, a durability test carried out for 700 h at 750 °C showed a remarkably stable performance of the fuel cell.

Introduction

In the intermediate temperature solid oxide fuel cells (IT-SOFC), the oxygen reduction reaction (ORR) and ion transport electrochemical reactions occurring at the cathode and cathode/electrolyte interface, are hindered when state-of-the-art (SoA) SOFC materials are used. It is precisely at this interface where phenomena of reactivity between phases and diffusion between cations occur, promoting the decrease in the fuel cell's performance and durability. Thus, the performance of the fuel cell will be greatly influenced by those interfaces. To achieve a high performance and durability of an IT-SOFC it is required to increase the cathodic activity and to decrease the interfacial resistance between cathode and electrolyte.

Currently, the LSCF perovskite cathode material reacts with the YSZ electrolyte (1–3), therefore doped-ceria barrier layer (BL) is introduced to inhibit the interdiffusion processes (4–9). However, there are still challenges for the optimization of the BL: its thickness must be minimized, and its microstructure and densification optimized to reduce ohmic resistance contribution. Pulsed laser deposition (PLD) has shown to be the most promising method to apply a thin dense, and continuous BL (10–12). Doped-ceria barrier layers deposited by PLD have improved the performance by 70% compared to SoA fuel cells and shown good stability under continuous operation (13).

Besides the BL, adjusted nanostructured layers can be deposited by the PLD technique to enhance the ORR by creating an interface rich of reaction sites. A possible strategy to increase the interface for ORR is to create a nanocomposite cathode combining an electronic conductor and ionic conductor. The strontium-doped lanthanum manganite (LSM), the standard cathode material for high temperature SOFC (800-1000 °C), is widely studied due to electronic properties, chemical stability, and specially its good compatibility with the YSZ electrolyte (14). However, due to its poor oxygen surface exchange and diffusivity causing a limited extension of reaction beyond the TPB, single-phase LSM is not an appropriate choice as a cathode when intermediate temperatures of operation are targeted (15) (16). The generation of nanocomposite electrodes combining structures of LSM with an ionic conductor such as samarium doped ceria (SDC) (17), which has a high oxygen conductivity, has been shown to increase the length of active area, and improve ORR kinetics (18).

The PLD method has been used to apply nano-scaled interlayers that accelerate the ORR kinetics and maximize the active interfacial area (19,20). Nanocomposite columnar structures have been grown between cathode and electrolyte as active functional layers (21) to decrease the overpotential by increasing the oxygen ion diffusivity, those nanocomposite layers have also shown enhancement in power density by improving adhesion properties, cause lattice distortions, increase oxygen vacancies and interfacial area density (18,22,23). Heterostructures affect the concentration and mobility of charge carriers near-interface phases and, consequently, the ionic and electronic properties of the material (24). The nanostructured interlayers appear to contribute significantly to affect the macroscopic electrochemical properties of the fuel cell and contribute to the improvement of the cell's performance and durability. While fuel cells comprising nanocomposite layers may exhibit enhanced power density by improving adhesion properties, increasing the density of the active surface area to facilitate the migration of oxygen ions, charge transfer processes, and long-term thermochemical stability remain a challenge (21,23,24). In this regard, a previous report investigated the fundamental electrochemical properties of LSM-SDC vertically aligned nanocomposites (VANs) deposited on model single crystal electrolytes (25). These VANs showed a greatly improved long-term thermal stability with respect to SoA electrode materials by suppressing the Sr segregation to the surface, along with enhanced oxygen kinetics as a consequence of fast diffusion and incorporation pathways promoted by the microstructural alignment (25). Moreover, unlike standard multilayer films, VANs are self-assembled structures, with stable interfaces formed at growth temperature, that exhibit good microstructural stability at operation temperatures.

In the present study an SDC barrier layer combined with an LSM-SDC nanostructured functional layer (NFL), both deposited by pulsed laser deposition (PLD), were applied in a reference anode supported cell. The role of such bilayer placed between the YSZ electrolyte and LSCF current collector layer (CCL) was investigated. The SDC BL will help minimizing cation interdiffusion while the composite's interface will enlarge the electrochemically active surface area for the ORR. The nanostructured layers applied by the PLD technique were fine-tuned to obtain dense and thin bilayers. The goal is to better understand the role of nanometric interlayers to enhance the overall performance of the cell and its durability.

Experimental

Pulsed laser deposition (PLD) of the barrier layer (BL) of SDC and of the nanofunctional layer (NFL) of LSM - SDC were performed on a multitarget chamber from PVD Products (PVD5000) with a KrF excimer laser ($\lambda = 248$ nm). The pressed targets used were of $Sm_{0.2}Ce_{0.8}O_{1.9}$ (Kceracell) for the BL and 50:50 wt% $(La_{0.8}Sr_{0.2})_{0.98}MnO_3$ (Kceracell) and $Sm_{0.2}Ce_{0.8}O_{1.9}$ (Kceracell) for the NFL target. An energy fluence of around 1 J.cm^{-2} was used for the ablation of the targets and a frequency of 10 Hz for the BL and of 2 Hz for the NFL. During the deposition process, the distance between the substrate and the target was 90 mm, the temperature of the chamber was kept at 750 °C under an oxygen partial pressure of 0.7 Pa.

The NFL and the BL+NFL were deposited by PLD on a 150 μm thick substrate of 8YSZ (Kerafol). The samples with only the NFL were treated at different temperatures, 900, 1000 and 1100 °C, to study the thermal stability of the NFL. Symmetric cells were prepared with the same set of deposition as described above on the 8YSZ substrate. A cathode layer of $(La_{0.6}\ Sr_{0.4})_{0.97}Co_{0.2}Fe_{0.8}O_3$ (Kceracell) was deposited on top of the as-deposited PLD layers on both sides of the cells by a 3-axis automated airbrush (Print3D Solutions). The samples with BL + NFL as interlayers were sintered at 1000 °C, found to be the optimal firing temperature for the LSCF attachment.

The crystalline phases of the as-deposited PLD layers and of the NFL submitted to different temperatures were characterized by X-ray diffraction (XRD) measurements on a Bruker-D8 Advance instrument at room temperature using Cu-Kα radiation with a nickel filter and a Lynx Eye detector. Initial microstructural analyses of the SDC BL and LSM-SDC NFL deposited on YSZ support with LSCF sintered at 1000 °C was carried out through transmission electron microscopy (JEOL 2010F TEM) of the lamellae of the cells prepared with the dual-beam instrument Helios 650.

The symmetric cells with the different interlayers and sintering temperatures were electrochemically characterized. The station used was the ProboStat™ (NorECS) which was placed inside a high-temperature vertical tube furnace. Au was used as the current collector and the impedance spectroscopy measurements (EIS) were carried out by the Novocontrol spectrometer (NOVOCONTROL Technologies GmbH & Co. KG) at the temperature ranging from 550 to 800 °C under the flow of synthetic air.

Complete SOFCs were prepared to evaluate the performance and the durability of a Ni-YSZ/YSZ/SDC/LSM-SDC/LSCF single cell. A reference half-cell supported by a Ni-YSZ anode (≈ 300 μm thick) and a 8YSZ electrolyte (≈ 7 μm thick) was used. The same deposition procedures, as described in the symmetrical cell, were used for the complete cell. Accordingly, the SDC barrier layer followed by the LSM-SDC ceramic nanocomposite layer were deposited by PLD on top of the electrolyte, and the LSCF cathode was airbrushed on top of the NFL and sintered at 1000 °C. A ProboStat™ (NorECS) system placed inside a high temperature tube furnace was used to test the complete cells. Ceramabond™ (Aremco) paste was used to seal the cell. The long-term durability test was done using a M9700 electronic load from Maynuo Electronic Co. Ltd. The measurements of the complete single cells were done under dry H_2 fuel in the anodic compartment and synthetic air in the cathode with a flow density of 22.22 Nml·min^{-1}·cm^{-2}.

The long-term durability test was carried out for 700 h at 750 °C under a current density of 0.3 $A \cdot cm^{-2}$.

Results and Discussion

The deposition of thin functional layers of the LSM-SDC (NFL) and SDC + LSM-SDC (BL + NFL) on YSZ substrates was carried out by the PLD method with a deposition temperature of 750 °C. X-ray diffraction patterns shown in Figure 1 exhibit the reported nanocomposite crystalline films on the YSZ substrate. It is possible to identify the cubic structure of the YSZ substrate and of the SDC. The LSM diffraction peaks match with its pseudo-cubic structure. Furthermore, an XRD analysis was carried out of the samples with LSM-SDC submitted to temperatures 900 – 1100 °C. It is possible to identify the YSZ, LSM and SDC phases in all samples and observe an increase in crystallinity as the temperature increases.

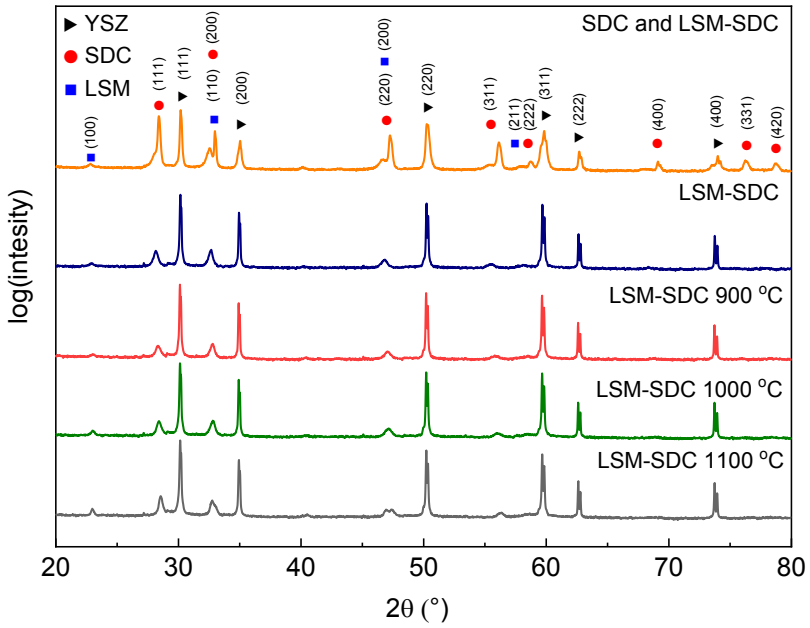

Figure 1. XRD patterns of PLD layers on YSZ: top to bottom: LSM-SDC as-deposited, and at 900, 1000 and 1100 °C

To determine the morphological characteristics of the final electrolyte-electrode interface microstructure, TEM cross-section images were obtained as shown in Figure 2. The TEM image shows the BL + NFL sandwiched between the YSZ substrate and airbrushed LSCF layer. The images show a 400 nm thick homogeneous bilayer of both SDC (200 nm) and LSM-SDC (200 nm). The layers exhibit high density and are well attached to both the YSZ electrolyte and the LSFC cathode.

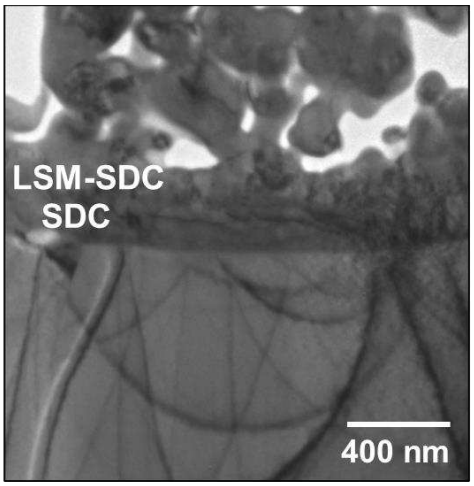

Figure 2. TEM image of the SDC BL and LSM-SDC NFL deposited on a YSZ support with LSCF sintered at 1000 °C.

The EIS analyses were firstly carried out of the samples with the configuration LSCF/LSM-SDC/YSZ/LSM-SDC/LSCF (Figure 3) treated at 900, 1000 and 1100 °C to define the optimal sintering temperature of the LSCF layer. Figure 3 (a) shows the impedance data at 750 °C. The experimental data were fitted with the here presented equivalent circuit $LR_S(R_{P1}CPE_{P1})(R_{P2}CPE_{P2})$. When describing the used elements, L refers to the inductive contribution due to the setup, R_S is the series resistance, ascribed to the ohmic contributions including the ionic resistance of the electrolyte and contact resistances. Finally, the electrode polarization resistance, the arcs at higher frequencies, were fitted with a resistance and a constant phase element (CPE) connected in parallel ($R_{Pi}CPE_{Pi}$).

The temperature dependence of the series (ASR_{series}) and polarization (ASR_{pol}) area-specific resistances for the different cells is reported in Figure 3 (b) and Figure 3 (c), respectively. The ASR_{series} was determined by the value of the fitting of the series resistance (R_s) in the EIS diagram, which is equivalent to the x-intercept at the high frequency end of the diagram. The ASR_{pol} was obtained from the sum of the polarization resistances (R_{p1} + R_{p2}) which are equivalent to the resistance of the two arcs in the EIS diagram.

Small differences between the ASR_{series} of the three samples were observed, and the same value of activation energy (E_a ~0.85 eV) was calculated. The samples treated at 1000 °C display the lowest resistance. Considering the ASR_{pol} the sample sintered at 1100 °C display a significant increase in the polarization resistance associated with a higher activation energy (E_a = 1.69 eV). Such resistive behaviour can be attributed to the high temperature sintering temperature of 1100 °C, which is known to promote the formation of resistive phases at the YSZ/LSCF interface (13). This high temperature coupled with the limitation due to the thickness of the layer (200 nm), might activate parallel interdiffusion processes between the cathode and the electrolyte leading to the formation of insulating phases and decomposition of the electrode material (10,26).

The lowest resistance at the cell operating temperature (~750 °C) was obtained by the heat treatment at 1000 °C. Thus, such a temperature was selected as the optimal one to produce the symmetrical cell with the additional SDC barrier layer and without any interlayer between the YSZ electrolyte and LSCF cathode (Figure 4).

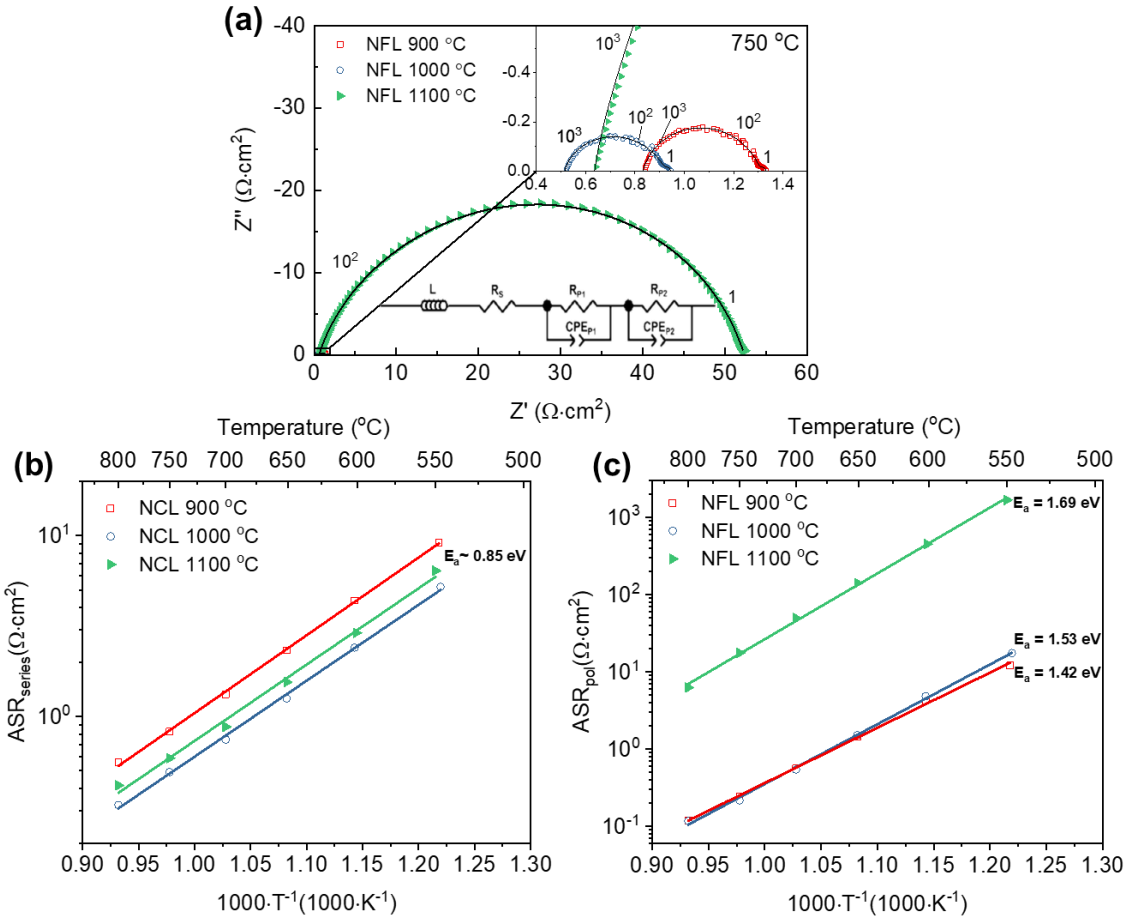

Figure 3. (a) EIS diagrams of the symmetrical cells with NFL (YSZ/LSM-SDC/LSCF) sintered at different temperatures measured at 750 °C. The inset shows the high-frequency portion of the diagrams and the equivalent circuit used to fit the impedance data. (b) and (c) Arrhenius plots of the series and polarization ASR, respectively, of the symmetrical cells.

The EIS diagram and the total area specific resistance (ASR_{total}) of the cells with the additional BL (LSCF/SDC/LSM-SDC/YSZ/LSM-SDC/SDC/LSCF) and without the bilayer (LSCF/ YSZ/LSCF) sintered at 1000 °C are shown in Figure 4 (a) and (b). The EIS data were fitted with the same circuit shown in Figure 3 (a). The cell without the bilayer exhibits more than a 40-fold increase in ASR compared to the cell with a bilayer (BL + NFL). This result emphasizes the importance of the ceria barrier layer to hinder the interface reactions between LSCF and YSZ.

Notably, the addition of an SDC BL (sample BL + NFL) was found to determine a significant decrease in the total resistance as compared with the sample with just the NFL. Such a decrease was associated with a greater impact on the polarization resistance, which decreased almost by an order of magnitude, as seen when comparing the impedance diagrams of the cells treated at the same temperature in Figure 3 (a) and Figure 4 (a). It is

observed that the most important difference is in the arc of polarization resistance formed at high frequency (R_{p1}). The R_{p1} value obtained from the fitted diagram is 0.43 Ω·cm^2 for the NFL at 1000 °C and 0.06 Ω·cm^2 when the SDC BL is added. The arc formed at high frequency can be attributed to interfacial impedance contributions at the electrode-electrolyte interface (27,28). It is assumed that the presence of the SDC BL favours oxygen ion transport from the electrode to the electrolyte.

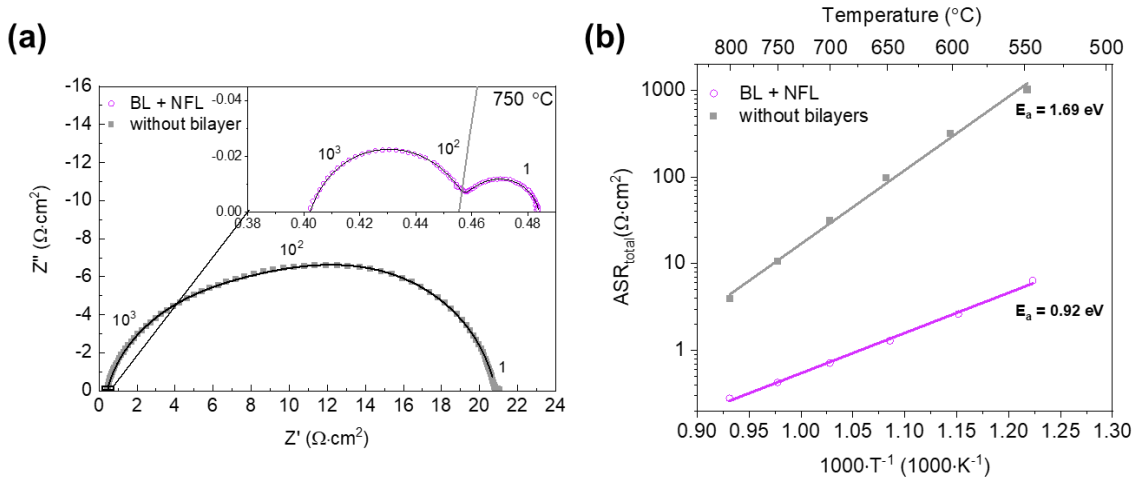

Figure 4. (a) EIS diagrams of the symmetrical cells with BL + NFL (YSZ/SDC/LSM-SDC/LSCF) and without the bilayer sintered at 1000 °C. The inset shows the expanded high frequency portion of the diagram. (b) Arrhenius plots of the total ASR of the symmetrical cells with NFL +BL and without the bilayer sintered at 1000 °C.

To evaluate the electrochemical performance of the fuel cell, an anode-supported single cell with the bilayer (BL + NFL) and LSCF sintered at 1000 °C was tested at 750 °C under dry hydrogen and synthetic air. A durability test shown in Figure 5 (a) was carried out for 700 h with a flow of 22 Nml·min^{-1}·cm^{-2} and a current density of 0.3 A·cm^{-2}. Remarkably, an improvement of 267 m·V·kh^{-1} was observed during the first 200 h of the test followed by a slight degradation of 41.9 m·V·kh^{-1} during the following 500 h. Throughout 700 h of operation, the fuel cell improved 225 m·V·kh^{-1}. The reported improvement in the cell provides evidence that the interfaces are still dynamic, and the nanostructured layers might have rearrangements leading the system to evolve towards a stable microstructure. Notably, a decrease in ASR for the LSM-SDC nanocomposite model system under thermal degradation (OCV conditions) was highlighted previously (25). Here, a similar behaviour is observed under SOFC operating conditions.

The voltage drops that occur after ~600 h in Figure 5 (a) can be possibly attributed to a crack in the ceramic sealing of the fuel cell allowing a change in the pO_2 of the chambers and could have a relation to the decrease in OCV after the 700-h test, as seen in Figure 5 (b). It can be seen from the I-V curve of Figure 5 (b) that the electrochemical performance of the cell was practically constant during the 700 h of operation. The fuel cell presents an OCV of 1.1 V as expected for the selected temperature range. The reported values on the I-V curve shows a maximum power density value of 0.30 W·cm^{-2} at 0 h and after 700 h

the maximum power density value has a slight increase to 0.31 W·cm^{-2} at 750 °C. Highlighting the remarkable stability of the cell during operation.

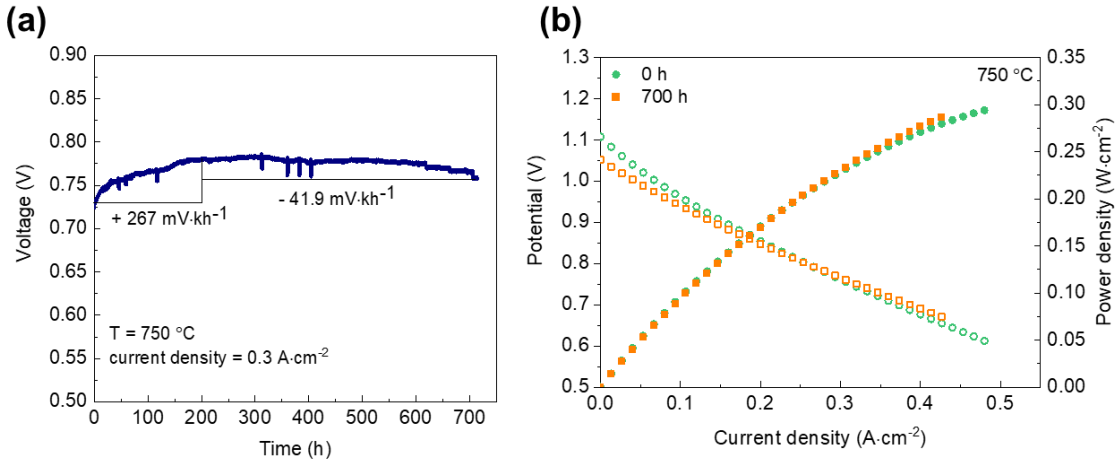

Figure 5 (a) Long-term durability test of the anode-supported single cell with the BL+NFL interlayers for 700 h at 750 °C, a current density of 0.3 A·cm^{-2}, under synthetic air and dry hydrogen, (b) I-V curves of the cell at 0 h and 700 h of operation measured at 750 °C under the same conditions.

Conclusions

Bilayers of Sm-doped ceria and LSM-SDC nanocomposites were successfully fabricated by the PLD technique. The layers showed a dense morphology with a thickness of ~200 nm each. The functional layers, upon optimization on symmetric cells, have been employed in anode-supported fuel cells, which demonstrated a stable performance through a durability test of 700 h with and an improvement of 225 m·V·kh^{-1} during operation. Such a performance enhancement can be arguably attributed to the rearrangement of cations in the interlayers. There is a synergistic contribution of an effective dense diffusion barrier that impedes undesired cation migration between the cathode and electrolyte interface. Along with a more efficient charge exchange promoted by the composite functional layer, in which having an assembly of an ionic conductor (SDC) with a typical electronic conducting phase (LSM) with rationalized microstructure, facilitates oxygen reduction reaction. The findings demonstrate that the combination of thin and dense barrier layers and a nanostructured cathode functional layer is an effective method for nanoengineering interfacial layers for high-performance durable solid oxide fuel cells.

Acknowledgments

Authors would like to acknowledge Brazilian agency FAPESP grants n° 2017/11937-4, 2019/04499-6 and 2022/06295-1. FCF is a fellow of the Brazilian CNPq. This project has received funding from the European Union's Horizon 2020 research and innovation program under grant agreement No 101017709 (EPISTORE).

References

1. S. Uhlenbruck, T. Moskalewicz, N. Jordan, H.-J. Penkalla, and H. P. Buchkremer, *Solid State Ion.,* **180**(4–5), 418–423 (2009).
2. G. Kostogloudis, *Solid State Ion.,* **135**(1–4), 529–535 (2000).
3. S. Simner, *Solid State Ion.,* **161**(1–2), 11–18 (2003).
4. A. Tsoga, A. Gupta, A. Naoumidis, and P. Nikolopoulos, *Acta Mater.*, **48**(18–19), 4709–4714 (2000).
5. A. Mai, V. Haanappel, F. Tietz, and D. Stover, *Solid State Ion.,* **177**(19–25), 2103–2107 (2006).
6. P. Plonczak , M. Joost, J. Hjelm, M. Sogaard, M. Lundberg, P.V. Hendriksen, *J. Power Sources,* **196**(3), 1156–1162 (2011).
7. L. dos Santos-Gómez, J. Hurtado, J. M. Porras-Vázquez, E. R. Losilla, and D. Marrero-López, *J. Eur. Ceram. Soc.,* **38**(10), 3518–3526 (2018).
8. Z. Gao, V. Y. Zenou, D. Kennouche, L. Marks, and S. A. Barnett, *J. Mater. Chem., A* **3**(18), 9955–9964 (2015).
9. C. Nicollet, J. Waxin*, T. Dupeyron*, A. Flura, J.-M. Bassat*, J. Power Sources,* **372**, 157–165 (2017).
10. M. Morales, V. Miguel-Perez, A. Tarancon, A. Slodezyk, M. Torrell, B. Ballesteros, J.P. Ouweltjes, J.M. Bassat, D. Montinaro, A. Morata, *J. Power Sources,* **344**, 141–151 (2017).
11. L. Bernadet, C. Moncasi, M. Torrell, and A. Tarancón, *Int. J. Hydrog. Energy,* **45**(28), 14208–14217 (2020).
12. R. Knibbe, *J. Am. Ceram. Soc.,* **93**(9), 2877–2883 (2010).
13. M. Morales, A. Pesce, A. Slodezyk, M. Torrell, P. Piccardo, D. Montinaro, A. Tarancon, A. Morata, *ACS Appl. Energy Mater.*, **1**(5), 1955–1964 (2018).
14. J. Kim, *Solid State Ion.,* **143**(3–4), 379–389 (2001).
15. S. Carter, A. Selcuck, R.J. Chater, J. Kajda, J.A. Kilner, B.C.H. Steele, *Solid State Ion.,* **53–56**, 597–605 (1992).
16. E. Ivers-Tiffée, A. Weber, and D. Herbstritt, *J. Eur. Ceram. Soc.,* **21**(10–11), 1805–1811 (2001).
17. J. Lane and J. A. Kilner, *Solid State Ion.,* **136–137**(1–2), 927–932 (2000).
18. Q. Su, D. Yoon, Z. SIsman, F. Khatkhatay, Q. Jia, A. Manthiram, H. Wang,, *Int. J. Hydrog. Energy,* **38**(36), 16320–16327 (2013).
19. Q. Su *et al.*, *J. Power Sources,* **218**, 261–267 (2012).
20. J. C. De Vero *et al.*, *J. Power Sources,* **377**, 128–135 (2018).
21. B. S. Kang, A. Inoishi, A. Takagaki, and T. Ishihara, *Solid State Ion.,* **327**, 59–63 (2018).
22. J. Yoon, S. Cho, J.-H. Kim, J. Lee, Z. Bi, A. Serquis, X. Zhang, A. Manthiram, H. Wang, *Adv. Funct. Mater.,* **19**(24), 3868–3873 (2009).
23. W. Ma, J.J. Kim, N. Tsvetkov, T. Daio, Y. Kuru, Z. Cai, Y. Chen, K. Sasaki, H.L. Tuller, B. Yildiz, *J. Mater. Chem., A* **3**(1), 207–219 (2015).
24. L. dos Santos-Gómez, S. Sanna, P. Norby, N. Pryds, E.R. Losilla, D. Marrero-Lopes, V. Esposito, *Nanoscale,* **11**(6), 2916–2924 (2019).
25. F. Baiutti, F. Chiabrera, M. Acosta, D.Diercks, D. Parfitt, J. Santiso, X. Wang, A. Cavallaro, A. Morata, H. Wang, A. Chroneos, J. MacManus-Driscoll, A. Tarancon, *Nat. Commun.,* **12**(1), 2660 (2021).
26. S. Molin, J. Karczewski, B. Kamecki, A. Mrozinski, S.-F. Wang, P. Jasinski, , *J. Eur. Ceram. Soc.,* **40**(15), 5626–5633 (2020).

27. S. B. Adler, *Chem. Rev.* **104**(10), 4791–4844 (2004).
28. J. T. S. Irvine, D. Neagu, M.C. Verbraeken, C. Chatzichristodoulou, C. Graves, M.B. Mogensen, *Nat. Energy,* **1**(1), 15014 (2016).